Preprints.org

Article

Not peer-reviewed version

Study on Effects of Modern Turbine Blade Coolant Injecting Nozzle Position on Film Cooling and Vortex Composite Performance under Rotating Conditions

Jiefeng Wang , Eddie Yin Kwee NG * , Jianwu Li , Yanan Huang , Yanhao Cao , Liang Li

Posted Date: 28 July 2023

doi: 10.20944/preprints202307.1983.v1

Keywords: Vortex cooling; Injecting nozzle location; Gas turbine; Blade film cooling; Heat transfer

Preprints.org is a free multidiscipline platform providing preprint service that is dedicated to making early versions of research outputs permanently available and citable. Preprints posted at Preprints.org appear in Web of Science, Crossref, Google Scholar, Scilit, Europe PMC.

Copyright: This is an open access article distributed under the Creative Commons Attribution License which permits unrestricted use, distribution, and reproduction in any medium, provided the original work is properly cited.

Preprints (www.preprints.org) | NOT PEER-REVIEWED | Posted: 28 July 2023 doi:10.20944/preprints202307.1983.v1

Disclaimer/Publisher's Note: The statements, opinions, and data contained in all publications are solely those of the individual author(s) and contributor(s) and not of MDPI and/or the editor(s). MDPI and/or the editor(s) disclaim responsibility for any injury to people or property resulting from any ideas, methods, instructions, or products referred to in the content.

Article

Study on Effects of Modern Turbine Blade Coolant Injecting Nozzle Position on Film Cooling and Vortex Composite Performance under Rotating Conditions

Jiefeng Wang [1], Eddie Yin Kwee NG [2,*], Jianwu Li [1], Yanhao Cao [1], Yanan Huang [1] and Liang Li [1,3,*]

[1] School of Energy and Power Engineering, Xi'an Jiaotong University, Xi'an 710049, China
[2] School of Mechanical and Aerospace Engineering, College of Engineering, Nanyang Technological University, 50 Nanyang Ave*Nu*e 639798, Singapore
[3] Shaanxi Engineering Laboratory of Turbomachinery and Power Equipment, Xi'an 710049, China
* Correspondence: author: mykng@ntu.edu.sg; liliang@mail.xjtu.edu.cn

Highlights

- The leading-edge cooling characteristics are studied in practical blade leading edge rather than symmetrical airfoil in previous studies on the vortex cooling technique.
- The effects of "asymmetrical property" of the vortex cooling flow field on the leading edge of the blade cooling structure under various rotational speeds are observed and analyzed.
- The Coriolis force is found as the root cause that influences the performance of the leading-edge cooling of the blade structure under various rotating speeds in different coolant injecting nozzle position cases.
- The composite cooling parameter with alterable weighting index which involves both heat transfer performance and working medium consumption is put forward to evaluate the performance of the composite cooling under difference preferences.

Abstract: This study investigates the effectiveness of the turbine rotating blade nozzle position on the characteristics of the vortex and film composite cooling numerically. The coolant injecting nozzles are set at the side of pressure surface (PS-side-in) .vs. that are set at the side of suction surface (SS-side-in) to compare the cooling characteristics at the rotating speed range of 0-4000rpm with fluid and thermal conjugate approach. Results show that the nozzle position presents different influences under low and higher rotational speed. As for the mainstream flow, rotation makes the stagnation line move from the PS-side pressure surface side to the SS-side suction surface side, which changes the coolant film attachment on the blade leading edge surface. The position of nozzles however indicates limited influence on the coolant film flow. As for the internal channel vortex flow characteristics, the coolant injecting from the nozzles forms a high-velocity region near the target wall which brings about enhancing convective heat transfer. The flow direction of the vortex flow near the internal channel wall is opposite and align to the direction of Coriolis force in both the PS-side-in and SS-side-in, respectively. Therefore, the Coriolis force augments to the convective heat transfer intensity of the vortex cooling in internal channel in SS-side-in while weakens the internal heat transfer in PS-side-in. Such effects become more intense with higher rotational speed. The blade surface area-averaged dimensionless temperature that inversely proportional to the actual temperature is 7.8% higher in SS-side-in as compared to that in PS-side-in. The SS-side-in suggests more superior composite cooling performance under the relatively higher rotating speed.

Keywords: vortex cooling; injecting nozzle location; gas turbine; blade film cooling

© 2023 by the author(s). Distributed under a Creative Commons CC BY license.

Preprints (www.preprints.org) | NOT PEER-REVIEWED | Posted: 28 July 2023 doi:10.20944/preprints202307.1983.v1

1. Introduction

Gas turbines have gained significant popularity in various applications such as aircraft, marine propulsions, and electricity generation, and they continue to undergo advancements. As one of the crucial factors contributing to the enhanced engine power and operating efficiency, the inlet temperature of the turbine part has surpassed to 1644-1700K. Consequently, the working conditions for turbine blades have become increasingly severe[1]. To counteract this challenge while minimizing coolant consumption, effective cooling methods have become imperative. Vortex cooling is a specialized approach for cooling the turbine blade leading-edge part. Vortex cooling combines the advantages of intense convective heat transfer observed in impingement cooling and the uniform heat flux distribution associated with axial flow. In practical scenarios, the blade leading edge cooling (such as vortex cooling) is usually utilized in conjunction with external film cooling (*EFC*) in the blade leading edge (*BLE*), and such a cooling method is called as the vortex and film composite cooling (*VFCC*)[1].

The heat transfer performance of composite film and vortex cooling is influenced by three primary factors. These factors encompass the geometrical parameters, the mass transfer between the internal vortex cooling (*IVC*) flow and the mainstream flow (*MF*), the heat transfer brought about by the blade material, and the aerodynamic factors (injection blowing rate ratio, rotational speed, temperature ratio, etc.). Researchers have conducted many studies on the *IVC* and *EFC* conception as cited in the following text.

In terms of *IVC*, earlier research mainly focused on the swirl-flow structure generation and measurement. Kreith *et al*.[2] combined the twisted tape with a cylinder channel to generate a swirl flow field with the axial inlet flow. They found that the swirl velocity reduced by 80-90% at around 50 times diameter downstream along the cylinder channel axis. Ling *et al*.[3] utilized the tangential nozzle and measured the target surface temperature using transient liquid crystal technique. Results showed that the Reynolds number of the coolant injecting flow led to distinct heat transfer intensity increment. Besides, the near-wall velocity distribution of the vortex flow field was measured in detail. Most of the recent studies on *IVC* focused on the influences of geometrical and aerodynamic factors on the *IVC* performance. Du *et al*.[6,7] established a *IVC* structure which consists a semi-cylinder, several tangential placed nozzles with a coolant inlet chamber. They systematically studied the influences of the jet nozzle aspect ratio, jet nozzle angle and jet nozzle amount on the flow and heat transfer characteristics of *IVC*. Fan *et al*.[6] experimentally tested the influences of the coolant inlet Reynolds *Nu*mber on the heat transfer intensity of the *IVC* structure put forward by Du *et al*.[4]. Wang *et al*.[7] found the mechanism of the vortex chamber cross-section area influence on the *IVC* characteristics.

As for *EFC*, researchers mainly focused on investigating the geometrical factors influences on the performance of the *EFC*. They also tried to introduce some special structures to optimize the *EFC* performance. Zhao *et al*.[8] utilized film holes to connect the internal axial flow cooling channel with the *MF*. They numerically compared the adiabatic *EFC* efficiency of the cylindrical film holes and fan-shaped film holes. Zhu *et al*.[9] numerically compared the showerhead *EFC* performance of the cylindrical film hole, fan-shaped film hole and the converging round-to-slot film hole in the *BLE*. Ye *et al*.[15,16] introduced the groove structure into the showerhead film hole on the *BLE* to optimize the *EFC* effectiveness.

In the previous work, it can be concluded that systematically and detailed investigations have been carried out separately on the *IVC* and the *EFC*. Whereas, the *IVC* and *EFC* are combined to cool the *BLE*. Although the internal cooling is involved in the research on the *EFC* above, the internal cooling in those studies is the axial flow cooling, which is different from the impingement cooling or the *IVC* in the practical *BLE*.

Some researchers focused on the *IVC* characteristics in the practical situations. In those studies, the *IVC* conception is placed in the *BLE*. Besides, they merged the film holes with the *IVC* structure to study the performance of the *VFCC*. Fan *et al*.[12] combined a row of film holes with the *IVC* structure and studied the film hole circumferential angle effect. Du *et al*.[13] numerically researched the rotation effects on the *IVC* based on the *VFCC* established by Fan *et al*. [12]. Li *et al*.[14] introduced

Preprints (www.preprints.org) | NOT PEER-REVIEWED | Posted: 28 July 2023 doi:10.20944/preprints202307.1983.v1

a rectangular channel as the airfoil cascade into the *IVC* model put forward by Fan *et al*. [12] and explored the *IVC* intensity as well as the adiabatic *EFC* effectiveness. Zhang *et al*.[15] experimentally explored the performance of the *VFCC* influenced by the *MF*. The *IVC* chamber was placed in a symmetrical *BLE*, where the *MF* flow field near the *BLE* was different from the practical situation. Wang *et al*.[16] numerically studied the nozzle position effect on the *VFCC* performance in a vane of GE E3 (General Electric Energy Efficient Engine). In that case, the *MF* flow field near the *BLE* was asymmetrical. And results showed that the position of internal coolant injecting nozzles would impact the heat transfer of the *IVC* and the coverage level of the *EFC*. However, the heat conduction of the blade material was not considered in their study.

From the foregoing discussion, most of the studies were linked to the impacting mechanism of aerodynamic and geometrical parameters on *IVC* performance. Nevertheless, there remains a limited number of investigations on predicting and analyzing the performance of *IVC* in *MF* cascades. *VFCC*, which combines *EFC* and *IVC*, is commonly employed to cool the *BLE* in the practical cases. The characteristics of the *VFCC* are dominated by the coverage of *EFC*, heat transfer of *IVC*, heat transfer through the blade material, and the effects of rotation. Nearly all the studies mentioned above used a semi-cylinder configuration to substitute the profile of the *BLE*, such as the experiment carried out by Zhang *et al*.[15]. In those simulations, the *MF* was symmetrical. However, it should be noted that the *MF* flow field in blade cascades is inherently asymmetrical. Therefore, those studies on the *MF* effects of the *VFCC* are quite different from the practical situation. In addition, the heat conduction through the blade material would connect the hot gas in the *MF* and the *IVC* flow. This heat conduction has a simultaneous impact on the heat transfer of the internal cooling and the effectiveness of the *EFC*. Consequently, it is essential to recognize that the fluid-thermal coupling simulating method is required which does not exist in the previous studies on the *VFCC*.

To further investigate the characteristics of the *VFCC*, it is imperative to conduct comprehensive investigations that consider asymmetrical *MF* effects, influence of the fluid-thermal coupling, and the effects of rotation and this is the strength or contribution of the current paper. A *VFCC* model is put forward and studied within the asymmetrical *MF*. Specifically, the structure of the *IVC* model is referred to the model in Du *et al*. [6,7] and Fan *et al*. [6]. The *MF* cascade structure and the blade profile are put forward based on the base stage1 blade in the test rig[17]. The *MF* flow field in the cascade will be asymmetrical. In our paper, the conjugate approach is carried out by introducing the blade material solid part to connect the *MF* flow field and the internal vortex flow field. The *VFCC* models with different coolant injection nozzle arrangements are established. The temperature distribution of the blade surface, the heat transfer distribution of the *IVC*, and the coolant film coverage of the *EFC* are calculated under different rotational speeds. This work might contribute to a more thorough understanding of the complex interactions of the *BLE* cooling and provide valuable references for the application of *IVC* in practical scenarios.

2. Materials and *Nu*merical Methods

2.1. Geometrical details

For convenience, the following technical phrases will be substitute to the respective abbreviations: internal vortex cooling (IVC), external film cooling (EFC), dimensionless temperature (delta), vortex and film composite cooling (VFCC), blade leading edge (BLE), mainstream flow (MF), SST k-ω with γ-θ transition model (SST~γ-θ), SST k-ω model (SST), the standard k-ω model (k-ω), and stagnation line (SL).

Figure 1 illustrates the three dimensional computational model. The boundaries are also be pointed out. The calculation model, as depicted in Figure 1 (a) and (b), comprises the cascade with the blade, film hole channels, IVC chambers, and the BLE material part of the blade as one integrated entity. The VFCC system consists of a inlet chamber connecting with a semi-cylinder vortex chamber (the connecting part consists of eight coolant injection nozzles) and twenity-four film holes channels (the coolant inside the vortex chamber could only enter the MF cascade through the film holes). The upstream and downstream segments is set to one and one point five times the length of the blade

Preprints (www.preprints.org) | NOT PEER-REVIEWED | Posted: 28 July 2023 doi:10.20944/preprints202307.1983.v1

chord, respectively. For clarity, Figure 1 presents only a partial view of the upstream and downstream segments. The extended upstream segment ensures the formation of the MF boundary layer before impacting the BLE surface.

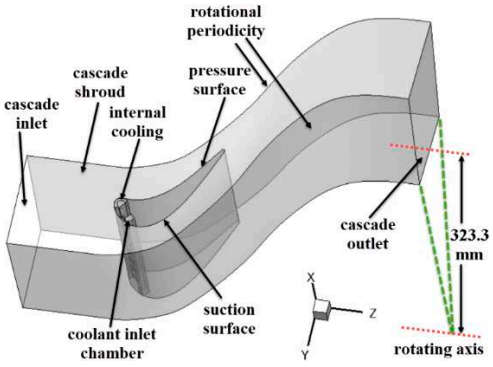

(a) cascade part of the three-dimensional computational model

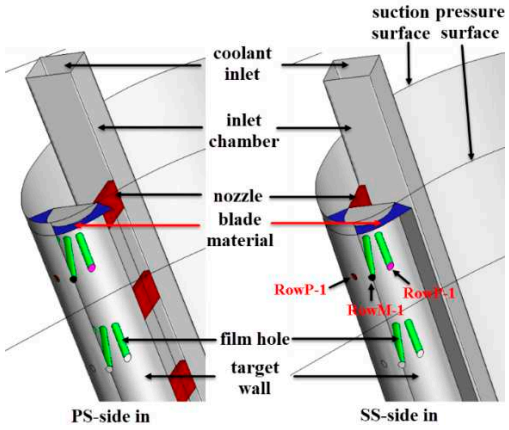

(b) *IVC* structure of the three-dimensional computational model

Figure 1. The three dimensional computational model.

Figure 2 presents the top view of the structure of the BLE of the blade. Given the IVC structure is asymmetrical compared to the classical symmetrical cooling conception such as impingement cooling, there are mainly two types of nozzle arrangements as indicated in Figure 2. The case in which the nozzles set near the side of pressure surface is called "PS-side-in" case, and the case in which the nozzles set near the side of suction surface is called "SS-side-in" case in the following text. In Figure 2 (b), there are two sections of the BLE: the segment of the pressure surface and the segment of suction surface. Our analysis primarily focuses on the isotherms distribution on the surface of the BLE, specifically on the suction surface leading edge part and the pressure surface leading edge part depicted in Figure 2 (b).

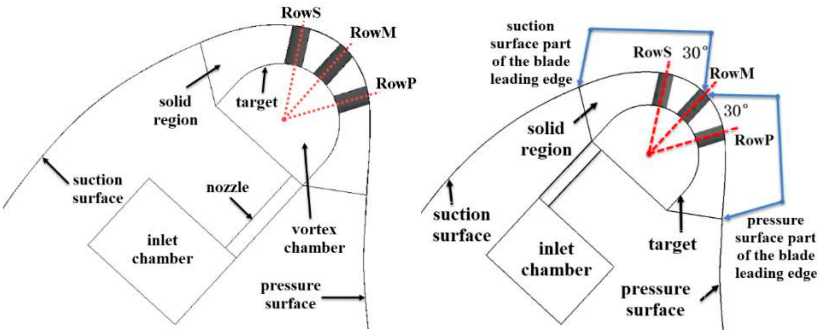

(a) PS-side in (b) SS-side in

Figure 2. Sketch of the two cases with different nozzle position.

Preprints (www.preprints.org) | NOT PEER-REVIEWED | Posted: 28 July 2023 doi:10.20944/preprints202307.1983.v1

Figure 3 exhibits the sizes of the vortex chamber of the VFCC model. The incline angle of the film holes with the showerhead configuration is set to 25°to blade height direction, with a 30° angle between adjacent rows of film holes (close to the GE E3 stage1 blade configuration[17]) as presented in Figure 2. Here, the inclined angle of 25° relative to the blade height is identical to the VFCC experiment with showerhead film holes[25]. Such an inclined angle setting of film hole configuration in the BLE is commonly applied in gas turbine blades as the coolant will be forced to move towards blade height direction due to the influence of the centrifugal force. The film hole channels at different height are labelled as Row1, Row2…Row8. Furthermore, the film holes located on the segment of the pressure surface, the segment of suction surface, and the position between them (Figure 2), are designated as RowP, RowS, and RowM, respectively. The entire computational model are rotational. The rotational axis is the Z-axis, with a length of 364mm[17] from the rotational axis to the hub wall of the cascade.

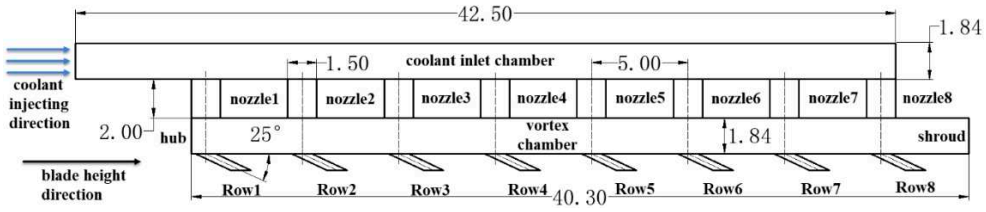

(a) side view of the internal vortex chamber

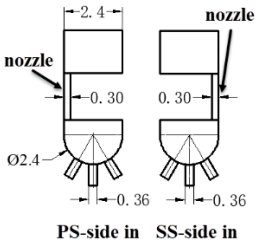

(b) front view of the internal vortex chamber

Figure 3. IVC structure sizes of the *VFCC* model.

As for the coolant flow path, the coolant initially blows into the inlet chamber from the boundary called internal inlet. Next, the coolant flows through the coolant injecting nozzles, and enters the vortex chamber as the tangential jet. Finally, the coolant flows through the film hole channels into the cascade, then becomes the film attached to the blade surface or mixes with the hot gas of the MF. As for the MF, in the stationary case, the MF hot gas flows into the cascade with an angle 30° to the Y-axis in the absolute coordinate. The MF inlet flow angle will gradually increases with the rising angular velocity. Such phenomenon will be discussed in Figure 7.

The profile of the blade, the configuration and sizes of the film holes, and the rotating axis setting in our setup are identical to the test rig used by NASA[17]. Furthermore, the IVC structure replicated and scaled from the experimental rig developed by Fan et al.[6].

2.2. Mesh generating

Figure 4 (a) and (b), displays a whole view and a partial view of the mesh, respectively. To generate the unstructured mesh with requested high-quality, the commercial software ANSYS 12.1 was utilized. The connecting surfaces between the solid domains and the fluid domains are set to the interfaces. In order to achieve low y^+ values, at least 12 prism layers were implemented in the regions near the boundary of the walls. Figure. 4 (c) presents the y^+ contour on the pressure surface under one of the calculating conditions. It could be captured that the y^+ is lower than 1 on the pressure surface of the blade. The y^+ values on other walls are all check to ensure y^+ is lower than 1. This approach ensures that the flow field in the regions near the wall is calculated directly rather than relying on empirical wall functions, by which the calcuating results will be much more accurate.

Preprints (www.preprints.org) | NOT PEER-REVIEWED | Posted: 28 July 2023 doi:10.20944/preprints202307.1983.v1

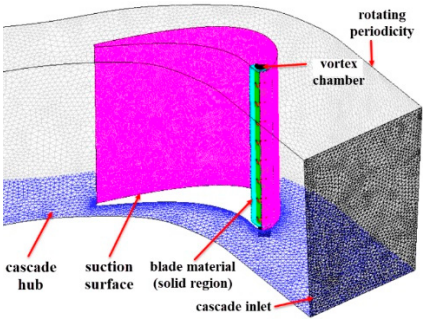

(a) mesh of the *MF* channel

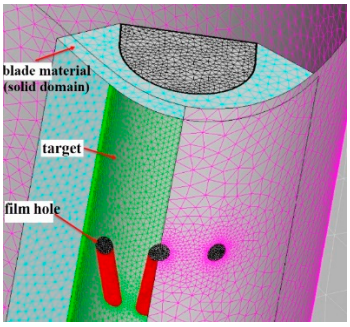

(b) mesh of the internal vortex chamber

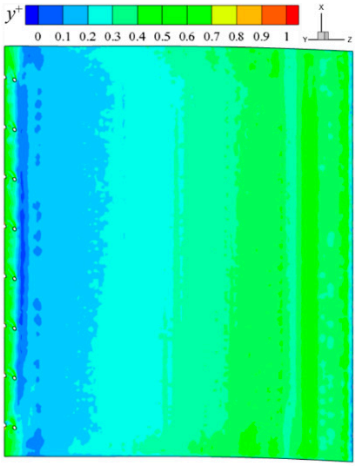

(c) y^+ contour on the pressure surface

Figure 4. Schematic of the calculating mesh and y^+ checking.

2.3. Solution procedure and boundary conditions

In the study conducted by Du et al.[13], the flow field and heat transfer distribution of IVC influenced by rotation were numerically investigated using the standard k-ω turbulence model coupled with the three-dimensional steady viscous RANS equation (Reynolds averaged Navier-Stokes). Similarly, Zhang et al.[15] and Wang et al.[16] examined the blade surface temperature, heat transfer intensity and flow field of the VFCC under the effect of the MF solving the RANS equation coupled with the realizable k-ε model or SST~γ-θ, respectively. These studies demonstrated that the two-equation turbulence models employed were effective in capturing flow field distribution and accurately simulating the distribution of the heat transfer affected by rotation. Consequently, our research also adopts the 3D steady viscous RANS model together with the turbulence model of two-equation for calculation, which applicable in engineering as the previous studies. If the hot spot in the MF inlet flow is involved, the transient unsteady simulation should be conducted to capture the interaction process between the coolant jet of the EFC flow and the hot spot.

Preprints (www.preprints.org) | NOT PEER-REVIEWED | Posted: 28 July 2023 doi:10.20944/preprints202307.1983.v1

For discretizing the convection term, we applied the high-resolution correction in the second-order format. Initially, the timestep is set to 10^{-4} s and is updated during iteration referring to the timescale factor value of 0.05. To ensure convergence, the monitors are set based on those critical variables throughout the iteration step. These variables include Reynolds numbers of the coolant inlet flow as well as the cascade inlet flow, the averaged target wall Nusselt number of the internal cooling chamber, the delta of area-averaged blade leading surface, and the film hole channel massflow rate.

The definition of Nusselt number Nu is identical with the previous studies on the IVC performance. The Nusselt Number Nu is defined as:

$$Nu = q_w D_c / (\lambda(T - T_w)) \quad (1)$$

where:

- q_w is the heat flux of the target wall shown in Figure 2 (W/m2)
- D_c means the cross section hydraulic diameter of internal vortex chamber (m)
- λ represents the fluid thermal conductivity (W/(m·K))
- T_w represents the target wall temperature

The dimensionless temperature θ is:

$$\theta = (T_\infty - T) / (T_\infty - T_c) \quad (2)$$

where(the following positions are given in Figure 1)

- T_∞ stands for the cascade inlet flow temperature
- T_c represents the coolant flow temperature of internal inlet

The higher θ indicates the lower actual temperature of the fluid or the blade wall. Convergence is achieved when the oscillation amplitude of the profiles of these variables' varying with the iteration step is lower than 5% of the average values.

Table 1 presents the boundary conditions set in the simulation. As for the MF cascade boundaries, the total temperature of the cascade inlet, the total pressure of the cascade inlet, and the static pressure of the cascade outlet are 206.431 kPa, 683 K, and 68.81 kPa, respectively. These values are obtained from experimental data in NASA experiment[17]. The turbulent intensity of the cascade inlet is set to a high level of 10%. As for the boundaries of the internal cooling chambers, the inlet total temperature is 352 K, while turbulent intensity of the internal inlet and the total pressure of the internal inlet are medium (5%) and 360 kPa, respectively. All the boundary conditions mentioned above are set based on the stationary coordinate (absolute coordinate). All walls are treated as the adiabatic and non-slip walls. The working medium is assumed to be the air ideal gas. The material of the solid is set as steel whose thermal conductivity is 60.5 W/(m·K) as the formula and property of the alloy of the gas turbine blade cannot be simply defined. The variation of the thermal conductivity versus temperature will be required if the researchers get interested, which is not the focus of the current research.

Table 1. Boundary conditions for simulation.

Region	Parameter	Value
MF cascade (fluid)	total temperature of cascade inlet (stationary)	683 K
	total pressure of cascade inlet (stationary)	206.431 kPa
	static pressure of cascade outlet (stationary)	68.81 kPa
	turbulence intensity of cascade inlet	high (10%)

Preprints (www.preprints.org) | NOT PEER-REVIEWED | Posted: 28 July 2023 doi:10.20944/preprints202307.1983.v1

internal chamber (fluid)	total temperature of internal inlet (stationary) turbulence intensity of internal inlet total pressure of internal inlet (stationary)	352 K medium (5%) 360 kPa
blade material (solid)	thermal conductivity of steel	60.5 W/(m·K)
	angular velocity ω	0, 500, 1000, 1500, 2000, 2500, 3000, 3500, 4000rpm

2.4. Grid independence analysis

To reduce numerical uncertainty and discretization errors, a grid invariant analysis is performed. This test helps determine the appropriate *Nu*mber of nodes for the simulation. In this analysis, the case with an angular velocity of 3000 rpm is selectedto conduct the grid independence analysis. There are three grids generated with the same growing rate at X-, Y-, and Z- directions, resulting in node numbers of 2.70 million, 7.42 million, and 18.79 million, respectively. All the three grids undergo smoothing, and the mesh quality standard are thoroughly checked prior to calculation.

The area-averaged delta on the suction surface part θ_S and the pressure surface part θ_P of the BLE (see Figure 2 (b)), along with the area-averaged Nusselt number on the target wall (see Figure 2 (b)) of the IVC chamber Nu_a, are calculateded and exhibited in Table 2. Additionally, Figure 5 illustrates the distribution of the coolant flow pressure in the vortex chamber, accompanied by the error bars of the numerical uncertainty. The grid with a node Number of 7.42 million is used for calculating the pressure distribution as shown in Figure. 5. The numerical uncertainty is evaluated using the GCI_{fine} method put forward by Celik et al.[18]. In their methods, an extrapolation value will be obtained by solving the GCI_{fine} equation utilizing the computational results calculated from a coarse, a medium and a fine grid. The numerical uncertainty is calculated based on the extrapolation value and with the results from those three grids. As shown in Table 2, the maximum numerical uncertainty not exceeding 5% of the pressure distribution solution.

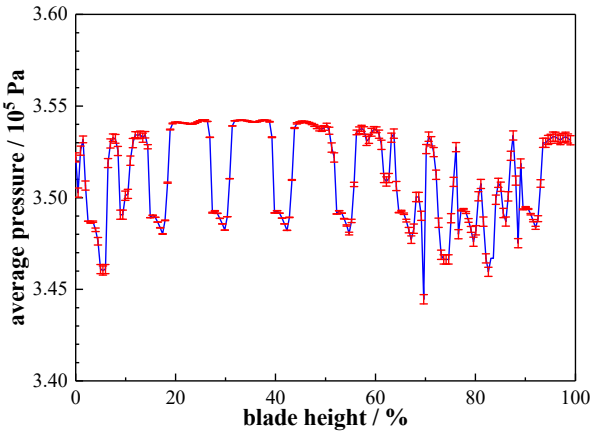

Figure 5. Profile of the coolant flow pressure in the vortex chamber along blade height with the numerical uncertainty.

Table 2. Numerical uncertainty (GCI) and extrapolation results calculated from the grid independence method.

Preprints (www.preprints.org) | NOT PEER-REVIEWED | Posted: 28 July 2023 doi:10.20944/preprints202307.1983.v1

Grid number (million)	Nu_a	θ_P	θ_S
2.70	65.76	0.4139	0.4163
7.42	65.26	0.4122	0.4161
18.79	67.20	0.4165	0.4206
Extrapolation	67.78	0.4190	0.4190
GCI	1.09%	0.75%	0.60%

2.5. Turbulence model verification

To obtain accurate and reliable numerical results, the selection of an appropriate turbulence model is crucial. Wang et al.[16] have demonstrated that the SST~γ-θ exhibits superior simulation accuracy to the SST and the k-ω, as illustrated in Figure 6. Figure 6(a) shows a flat board film cooling experiment carried out by Kohli et al.[19], where the SST~γ-θ demonstrates superior performance in predicting the distribution of the film cooling eeffectiveness. This model accurately captures the laminar-to-turbulent transition at the downstream region of the film hole.

In Figure 6(b) and (c), a comparison is shown between simulation and experimental data from the NASA GE E3 experiment[17]. All the three turbulence models adequately predict the distribution of the vane efficiency. However, discrepancies between the numerical results and experimental data become more pronounced within the blade height range of 5% to 40%. Such a phenomenon may be attributed to non-uniform inlet flow field conditions or fluctuations in inlet flow velocity during the experiment.

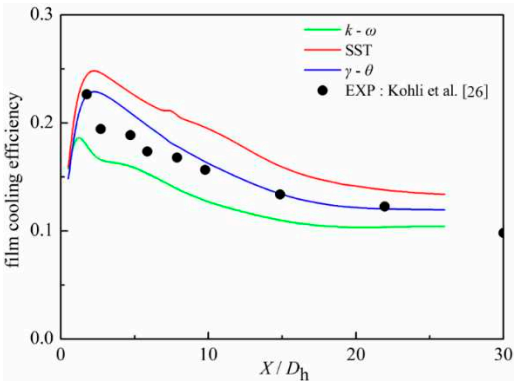

(a) Simulation results compared with the experimental data of the film cooling effectiveness

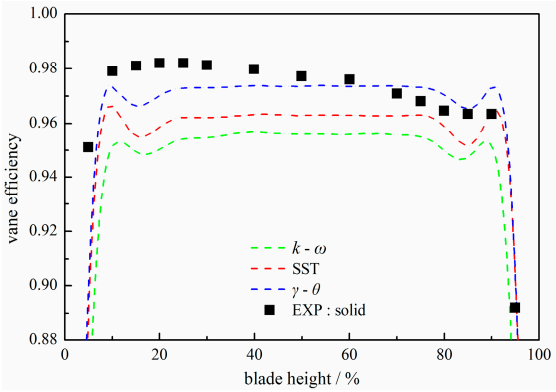

(b) Simulation results compared with the experimental data of the vane efficiency in the solid airfoil experiment

Preprints (www.preprints.org) | NOT PEER-REVIEWED | Posted: 28 July 2023 doi:10.20944/preprints202307.1983.v1

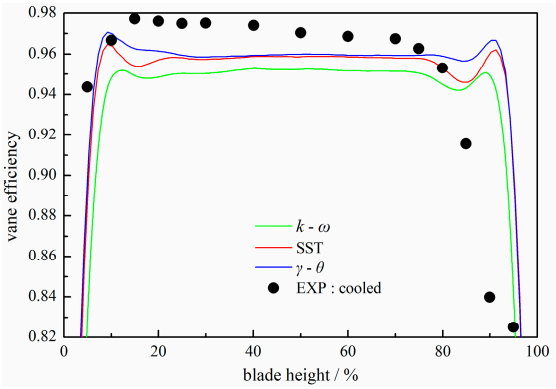

(c) Simulation results compared with the experimental data of the vane efficiency in the cooled airfoil experiment

Figure 6. Comparison of the prediction data obtained from the turbulence models to the experiment data [24].

3. Results and discussion

In a study by Safi *et al*.[20], a *Nu*merical investigation was conducted to explore the rotational influences on the impingement cooling performance in the *BLE* of gas turbines. The simulations covered a rotating speed range of 0-750 rpm, revealing the underlying mechanism of rotational influences on the *VFCC* performance in the *BLE* of gas turbine. In the current research, similar simulations are performed within an extended rotating speed range of 0-4000 rpm, which aligns with the range studied by Safi *et al*.[20].

3.1. Rotation influences on the external flow

Figure 7 shows the sketmatic figure of the direction of the *MF* inlet flow versus the angular velocity. There are three types of velocity vector: the *MF* inlet flow absolute velocity $\boldsymbol{c}$, the angular velocity $\boldsymbol{u}$ and the *MF* inlet flow velocity relative to the rotation frame w, in which $\boldsymbol{c}= \boldsymbol{u} + \boldsymbol{w}$. When the angular velocity u is 0rpm, velocity c and velocity $\boldsymbol{w}$ are identical. The angle between the velocity w and Y- axis is 30°. As the angular velocity $\boldsymbol{u}$ increases under the fixed velocity $\boldsymbol{c}$, the angle between the velocity $\boldsymbol{w}$ and Y- axis gradually increases. A flow stagnating to the blade will bring about a line-shaped stagnation region on the *BLE* surface, whose position is related to the flow direction. Given the blade could be regarded as a rotation frame, it can be concluded in Figure 7 that the stagnation region will move from the pressure surface side to the suction surface side on the *BLE* surface with the increasing angular velocity $\boldsymbol{u}$. Such a phenomenon can be seen in Figure 8. The line-shaped stagnation region is termed "*SL* (stagnation line)" in the following text.

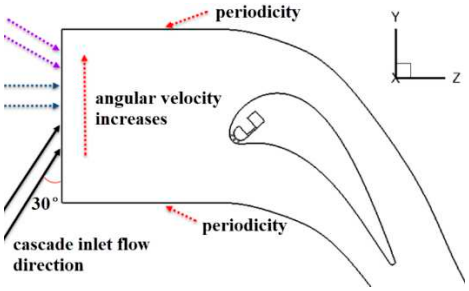

Figure 7. Schema of transfer learning technique with pre-trained models for binary classification.

Figure 8 illustrates the pressure contour and surface streamlines on the *BLE*. The presence of *SL*s could be observed as characterized by the opposite streamline directions on each side of these lines. At 0 rpm, the *SL* presents a relatively straight profile from hub to shroud side and is positioned to the left side of RowP. When the rotating speed rises, the *SL* shifts towards the suction surface of the

Preprints (www.preprints.org) | NOT PEER-REVIEWED | Posted: 28 July 2023 doi:10.20944/preprints202307.1983.v1

blade and eventually settles on the left of film hole RowS. This shift is attributed to the keeping growing norm of the circumferential velocity $\boldsymbol{u}$ as presented in the velocity triangle, leading to a direction change in the of $\boldsymbol{w}$, as explained in Figure 7. Metaphorically, the upper portion of the *SL* moves "faster" towards the blade suction surface compared to the portion near the hub with increasing rotating speed, primarily due to the higher circumferential velocity near the shroud. This difference becomes more distinct at higher rotating speeds. Additionally, the surface streamlines gradually curve towards the side of the shroud given the effects of the growing centrifugal force associated with the growing rotational speed. It is worth noting that the position of the *SL* aligns with RowP and RowM positions at 1500 rpm, 3000 rpm and 3500 rpm, respectively. The position of the *SL* will affect the heat and mass transfer between the coolant film flow and the *MF*.

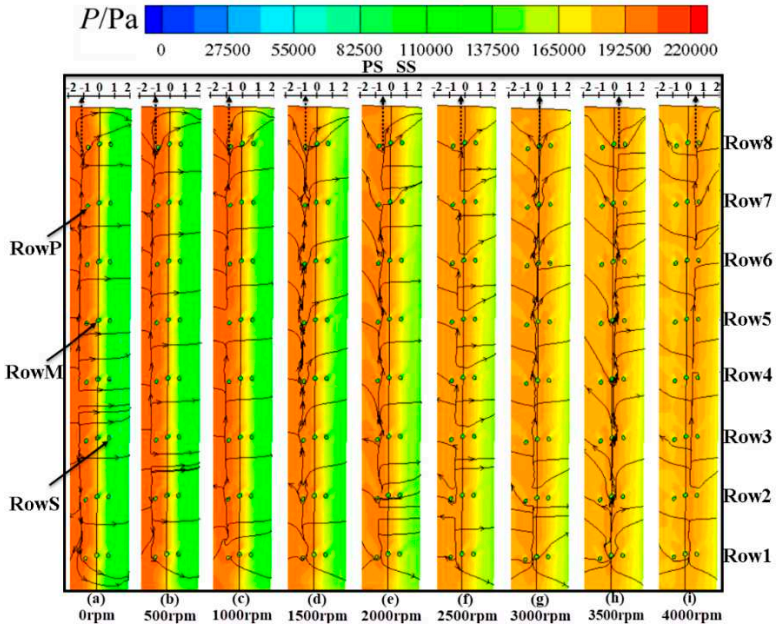

Figure 8. Pressure contour and surface streamline on the leading-edge region of the blade under all rotating speeds.

Figure 9 presents the blowing ratio variation versus the rotating speed in PS-side-in and SS-side-in. Referring to Figures 2, RowP-6, RowM-6 and RowS-6 represents the sixth-row of film hole locates at the pressure surface, the suction surface, and the position between the suction surface and pressure surface, respectively. In general, the blowing ratios of those three film holes fluctuant increase with the growing rotational speed. Such a phenomenon is brought about by the enlarging centrifugal force caused by the increasing rotating speed, which as a result, forces the coolant to move along the blade height direction. It is noteworthy that, the blowing ratios of RowP-6 and RowM-6 at 0-1000rpm are lower in PS-side-in than that in SS-side-in. The reasons are explained as following. On the one hand, the coolant injecting nozzles stay closer to RowP in PS-side-in than SS-side-in as can be seen in Figure 2. Hence, more coolant will flow to the *MF* through RowP in PS-side-in than the SS-side-in. On the other hand, the *SL* appears near RowP and RowM at 0-1000rpm as indicated in Figure 8, which brings about higher *MF* pressure near RowP and RowM but lower *MF* pressure near RowS. In that case, in SS-side-in, higher proportion of the coolant directly flows into the *MF* through RowS rather than RowP or RowM. This causes a lower blowing ratio of RowP and RowM as well as a higher blowing ratio of RowS in SS-side-in compared to PS-side-in at 0-1000rpm. Such phenomena will bring about the difference for the performance of the *VFCC* in the following discussion.

Preprints (www.preprints.org) | NOT PEER-REVIEWED | Posted: 28 July 2023 doi:10.20944/preprints202307.1983.v1

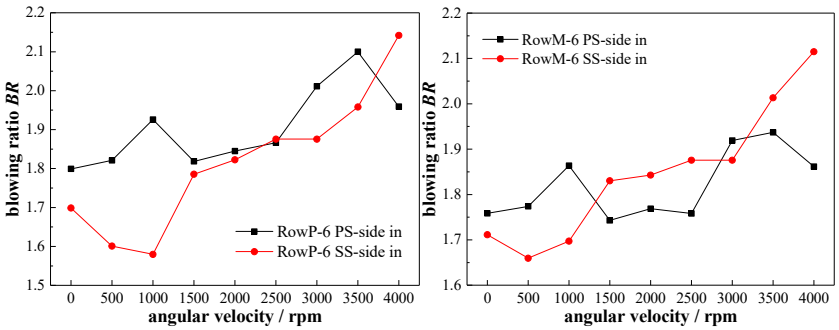

(a) RowP-6 (b) RowM-6

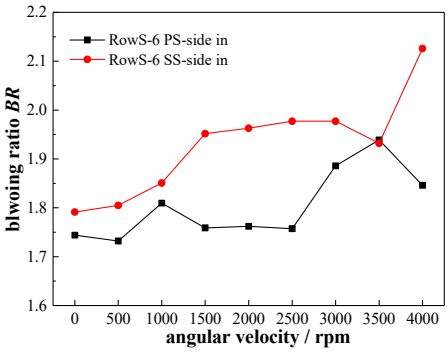

(c) RowS-6

Figure 9. Blowing ratios of the film holes Row6 under all rotating speeds.

Figure 10 depicts different types of cross-sections for analysis in Figures 11, 14 and 15. Section A presented in Figure 10 (a) locates on the axis of RowM and is parallel to the blade height. There are three types of section A. They locates on the axis of RowP, RowM and RowS, respectively. Section A is created to 'capture' the external near wall flow field of the *EFC* as presented in Figure 11. Section B shown in Figure 10 (b) locates on the blade height of Row6 and is vertical to the blade height to 'capture' the flow field of the *IVC* in Figures 14 and 15.

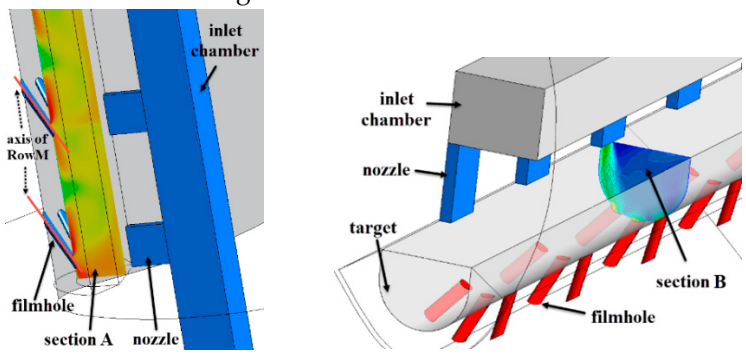

(a) section A presented in figure. 11 (b) section B presented in figure. 14 and figure. 15

Figure 10. Schema of transfer learning technique with pre-trained models for binary classification.

Figure 11 presents the θ contour on section A as presented in Figure 10 (b) to exhibit the spreading level of the coolant film on the blade surface. Figures 11 (1), (2) and (3) illustrate the local-region θ contour near RowP-6, RowM-6 and RowS6 in PS-side-in and SS-side-in, respectively. In general, there are mainly three types of *EFC* flow regimes under all of the rotating speed scenarios. First, the coolant jet lifts away from the surface of the blade and penetrates into the *MF*, such as the phenomena revealed in Figures 11(2)(a), 11(3)(d) and 11(4)(f). The coolant jet lifting off is caused by the low *MF* pressure at the outer side region of the film hole and the higher blowing ratio of the film

Preprints (www.preprints.org) | NOT PEER-REVIEWED | Posted: 28 July 2023 doi:10.20944/preprints202307.1983.v1

hole. In that case, the coolant film thus fails to protect the blade surface from the *MF* hot gas sufficiently. Second, the coolant jet is suppressed by the *MF* to the surface of the blade and spreads on the blade surface. This phenomenon appears when the position of the *SL* aligns with the film hole position as presented in Figure 8. At 1500rpm, the *SL* stays at the position of RowP. Given the pressure and temperature of the *MF* near the *SL* position is the highest within the whole fluid domain, the coolant jet from RowP is suppressed onto the blade surface, leading to a large coolant film coverage area on the blade surface as seen in Figure 11(2)(c). Similarly, the coolant film from RowM attaches to the surface of the blade well at 3000rpm as reveled in Figure 11(3)(e). Third, the coolant jet lifts off initially and then reattachment to the surface of the blade as shown in Figures 11(2)(f), 11(3)(a) and 11(4). The reattachment level is affected by both the stagnation position and rotating speed. The increasing centrifugal force as a result of the increasing rotating speed makes the coolant film flow towards the side of the shroud, therefore increasing the reattachment distance as seen in Figure 11(4). Furthermore, the *SL* gets closer to film hole RowS with an increasing rotating speed. The high-pressure hot gas of the *MF* flow around the *SL* then pushes the coolant jet away and increases the reattachment zone.

The coolant film flow distribution in PS-side-in is rather similar to that in SS-side-in, especially at the rotating speed higher or equal to 1000rpm. At 0rpm or 500rpm, the coolant film from RowM shows higher attachment level in PS-side-in compared to SS-side-in. Because the value of blowing ratio of RowM in PS-side-in is higher than that in SS-side-in as presented in Figure 9(b). Higher blowing ratio of RowM indicates that larger amount of coolant reattaches to the surface of the blade. In general, the coolant film attachment levels in PS-side-in and SS-side-in under the identical rotating speed are almost the same. This suggests that there's little difference of the *EFC* effectiveness between PS-side-in and SS-side-in.

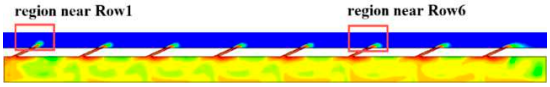

(1) The local regions presented in figure 12 (2), (3) and (4)

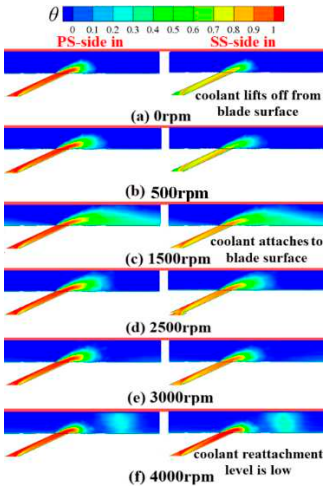

(2) contour of *delta* in the near wall region of RowP-6

Preprints (www.preprints.org) | NOT PEER-REVIEWED | Posted: 28 July 2023 doi:10.20944/preprints202307.1983.v1

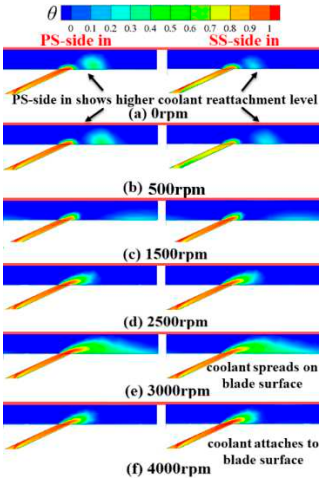

(3) contour of *delta* in the near wall region of RowM-6

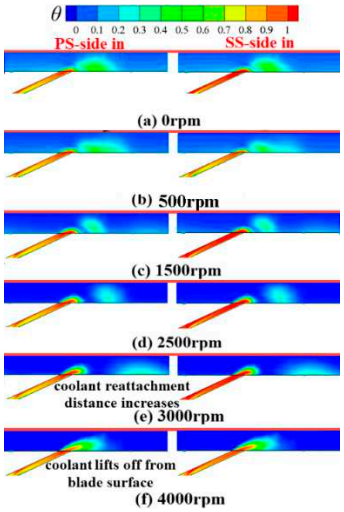

(4) contour of *delta* in the near wall region of RowS-6

Figure 11. Near-wall contour of *delta* on the cross-section A presented in figure 10(a).

Figure 12 presents *delta* (defined in eq(2)) contour on the *BLE* surface of the PS-side-in and SS-side-in under all rotating speed range. In general, there are distinct differences on the temperature distributions on the *BLE* between the PS-side-in and the SS-side-in. Whereas the coolant film coverage situations on those two cases are quite similar as plotted in Figure 11. This concludes that the dominating factor that brings about such temperature distribution differences is related to the *IVC* rather than the *EFC*.

As for the similarities, large-area of the low-temperature regions could be captured at 1500rpm, 3000rpm and 3500rpm, in which the position of the *SL* aligns with the film hole position. Large-area of coolant film coverage brings about large-area of low temperature regions. When the *SL* exists at other positions, the coolant film is pushed away by the high-pressure *MF* near the *SL*, leading to a higher area-averaged temperature on the *BLE* surface.

As for the differences, there are mainly three aspects of dissimilarities between the PS-side-in and the SS-side-in. First, the blade surface temperature is much higher in SS-side-in than that of the PS-side-in when the rotating speed is lower or equal to 1000rpm. Second, the blade surface temperature in SS-side-in becomes higher than that in the PS-side-in when the rotating speed is higher than 1500rpm. Such a variation becomes larger with the increasing rotating speed. Those phenomena could also be captured in Figure 13, which shows the area-averaged *delta* (θ_a) on the *BLE* surface under all rotating speeds. The highest differences appear at 0rpm and 3500rpm, where θ_a in PS-side-in is 37.3% higher than the SS-sid-in and θ_a in SS-side-in is 7.8% higher than that in PS-side-in, respectively. Third, there are large-area of high-temperature regions appear near the shroud in

Preprints (www.preprints.org) | NOT PEER-REVIEWED | Posted: 28 July 2023 doi:10.20944/preprints202307.1983.v1

the PS-side-in at 1000-3500rpm. Nevertheless, those high-temperature regions disappear in the SS-side-in.

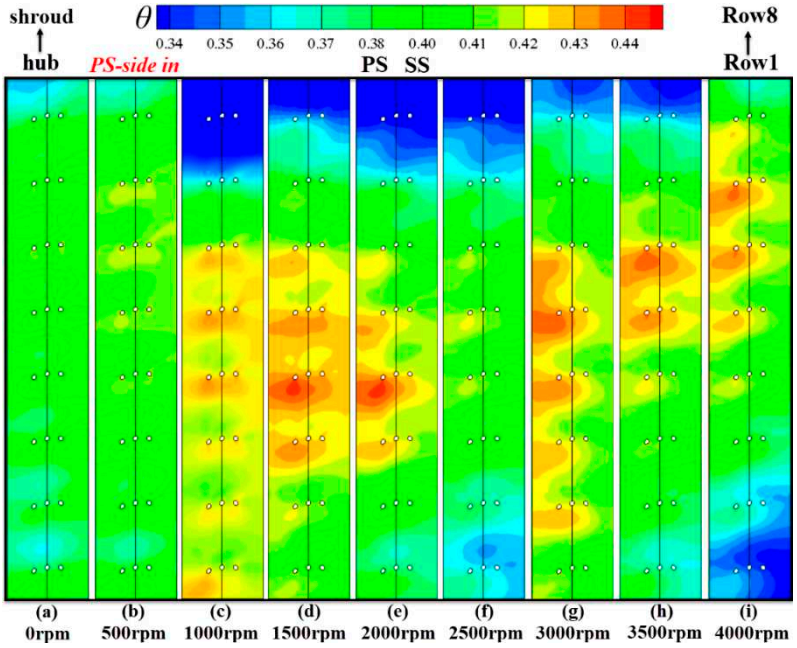

(1) PS-side in

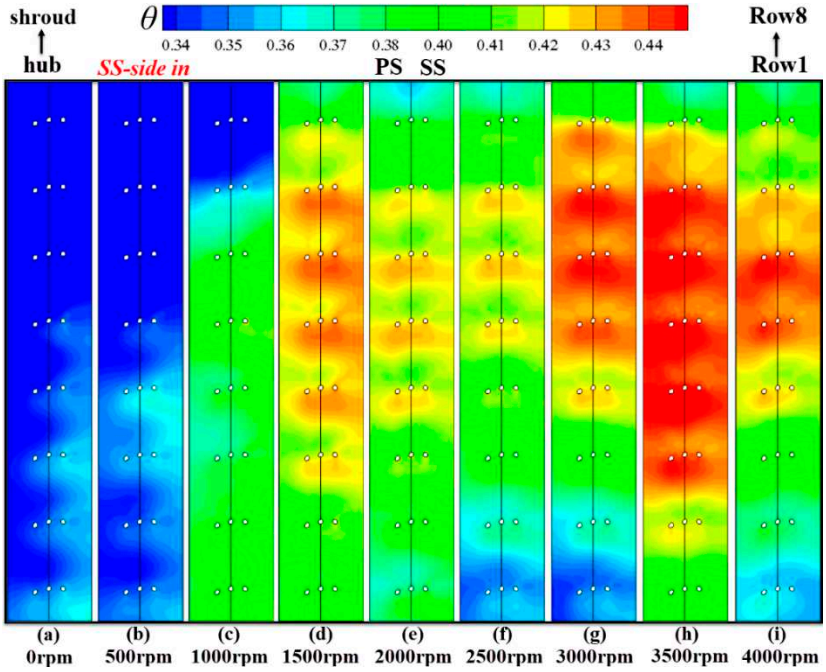

(2) SS-side in

Figure 12. Contours of *delta* on the *BLE* surface under all rotating speeds.

Preprints (www.preprints.org) | NOT PEER-REVIEWED | Posted: 28 July 2023 doi:10.20944/preprints202307.1983.v1

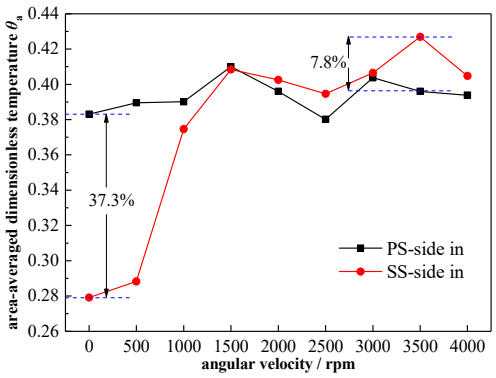

Figure 13. Area-averaged *delta* on the *BLE* surface under all rotating speeds (PS-side-in .vs. SS-side-in).

In summary, the arrangement of the internal coolant injecting nozzles confirms little influence on the flow field of the *EFC*. However, the nozzle arrangement presents significant influences on the temperature of the *BLE*. This indicates that the nozzle configurations will change the *IVC* performance, and then affects the *VFCC* performance. The discussion on the *IVC* is presented next.

3.2. Rotation influences the on IVC flow

The rotation influences on the flow field of the *IVC* are discussed in Figures 14 and 15. Figure 14 shows contour of velocity V_{yz} as well as the streamline on the Y-Z section as presented in Figure 8 (c). V_{yz} is defined as:

$$V_{yz} = (V_y^2 + V_z^2)^{0.5} \quad (3)$$

where

V_y stands for the Y- component of the coolant velocity in the rotational frame

V_z stands for the Z- component of the coolant velocity in the rotational frame

As can be seen in Figure 14, the coolant blows into the vortex chamber tangentially and scours the target surface. The coolant flow 'crashes' the target surface and forms large-scale vortices, leading to intense convective heat transfer on the target wall. A high-velocity region near the target wall and a low-velocity region in the core region of the vortex chamber are formed. Position of the target wall is indicated in Figure 2. Then the coolant flows towards the *MF* through the showerhead film holes drove by the relatively larger pressure difference between the vortex chamber and the cascade, which is pointed out as the 'suction effect' by Fan *et al*.[12]. Such a 'suction effect' changes the position and the intensity of the vorticity of the large-scale vortex in the vortex chamber. In addition, the coolant flow will be accelerated by the 'suction effect', which will augment the heat transfer intensity around the region near the film holes. As the intensity of the 'suction effect' is dominated by the position of the stagnation point as presented in Figure 14.

When the rotating speed is relatively low, particularly at 0-500rpm, the stagnation point stays near RowP, bringing about higher-pressure and lower-pressure at the outer region of RowP and RowS. Therefore, high proportion of the coolant from the nozzle directly flows into the *MF* through RowS in SS-side-in rather than flows along the target wall. As for PS-side-in, relatively low proportion of the coolant from the nozzle flows into RowP. Some coolant is forced by the suction effect of RowS and flows downstream along the target wall. Such a phenomenon is more distinct as revealed in Figure 15, that presents the velocity contour and streamline on the cross-sections at various blade height at 0rpm. It can be concluded that, the much more intense "suction effect" of RowS in SS-side-in makes the large-scale vortex losing its original shape. The flow field in the vortex chamber in SS-side-in is more chaotic than that in PS-side-in. Therefore, the intensity of the internal heat transfer in SS-side-in will be much lower than that in PS-side-in. This conclusion could be captured in Figure 17, which shows the area-averaged *Nu*sselt *Nu*mber *Nu*a on the target surface. The value of *Nu*a in PS-side-in is 52.6% higher than the SS-side-in. The low the intensity of the internal

Preprints (www.preprints.org) | NOT PEER-REVIEWED | Posted: 28 July 2023 doi:10.20944/preprints202307.1983.v1

heat transfer explains well the reason why the blade surface temperature in SS-side-in is much higher at 0-500rpm than that in PS-side in as seen in Figures 12(a) and (b).

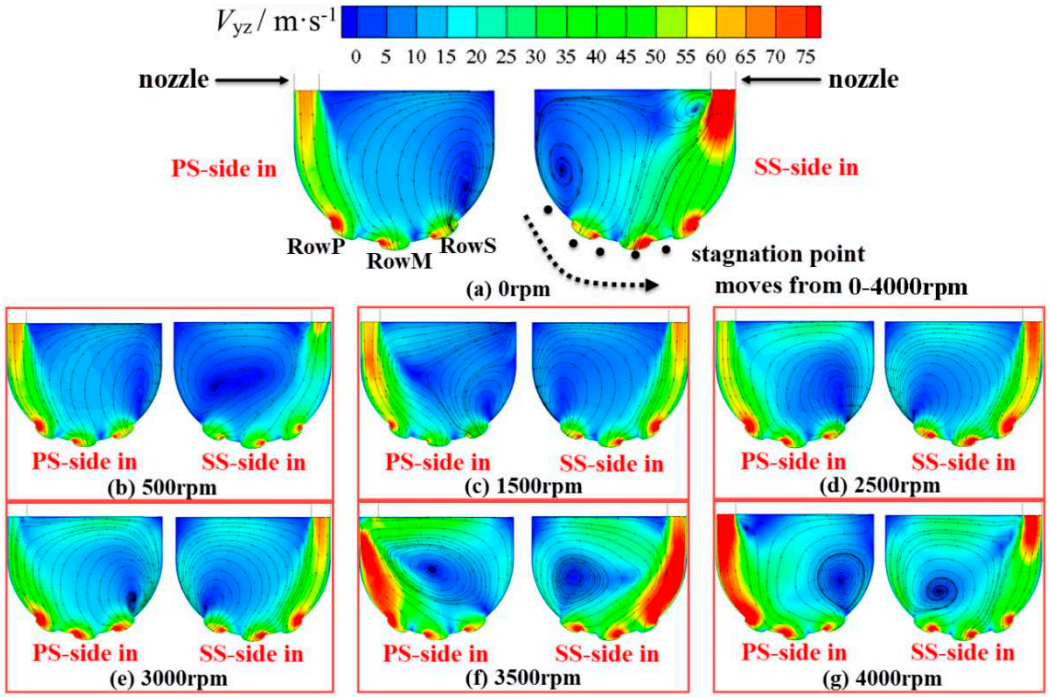

Figure 14. Schema of transfer learning technique with pre-trained models for binary classification.

When the rotating speed is higher than 1500rpm, there's an opposite result in internal heat transfer intensity. The intensity of the internal heat transfer in SS-side-in becomes higher than the PS-side-in. Such a phenomenon could be observed in Figure 14. In Figures 14 (d)~(f), the high-velocity near wall region originating from the nozzle covers a larger area in SS-side-in than that in PS-side-in. There are mainly two reasons. Firstly, as the rotational speed gradually grows to 3500rpm, the stagnation point gradually moves towards the position near RowS, leading to a relatively higher-pressure and lower-pressure at the outer side of RowS and RowP. As for the PS-side-in, high proportion of coolant from the nozzle directly flows into RowP rather than flows downstream along the target wall. For the SS-side-in, relatively low proportion of coolant from the nozzle flows into RowS, and some coolant flows downstream along the target wall. Hence, the high-velocity near wall region in SS-side-in covers a relatively larger proportion of the target wall than that in PS-side-in, allowing a larger intensity of the heat transfer of the *IVC* in SS-side-in compared to PS-side-in.

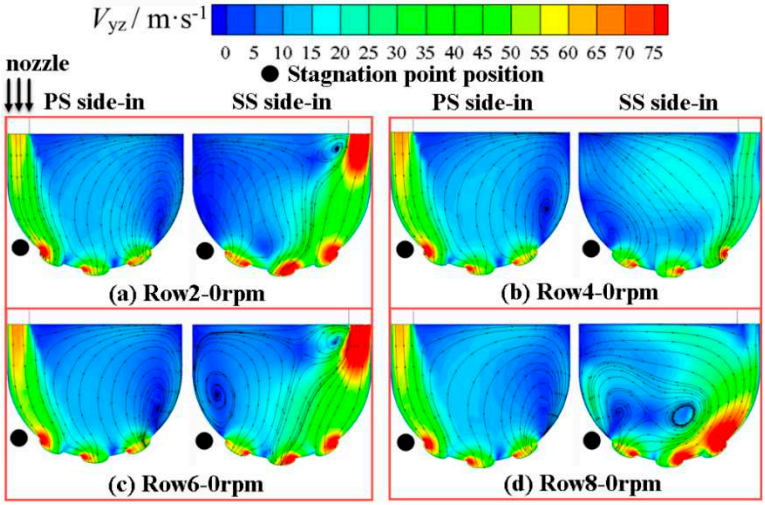

Preprints (www.preprints.org) | NOT PEER-REVIEWED | Posted: 28 July 2023 doi:10.20944/preprints202307.1983.v1

Figure 15. Streamline and contour of velocity on the cross-section B presented in figure 10(b) at various blade heights under 0rpm.

Secondly, the differences of the internal vortex flow field between the PS-side-in and the SS-side-in are related to the centrifugal force and the Coriolis force brought about by the rotation. Figure 16 exhibits the sketch of the Coriolis force effect on the internal vortex flow. Figure 16(b) shows the direction of the centrifugal force and the axial velocity. The rotation brings about the centrifugal force towards the blade height direction, which forces the coolant flows towards shroud and forms the axial velocity V_r. The higher rotating speed leads to the higher axial velocity V_r. As seen in Figures 16(a) and (c), the red dotted line represents the direction of the angular velocity ω. Therefore, based on the equation $F_c=-2\omega\times V_r$, the Coriolis force Fc could be represented by the blue dotted line. The higher rotating speed leads to the ω and V_r, which permits higher Coriolis force Fc. In terms of the PS-side-in, the direction of the Coriolis force F_c is nearly opposite to the near wall vortex flow direction, that prevents the high-velocity coolant near the target wall developing downstream. In terms of the SS-side-in, the direction of the Coriolis force F_c is like the near wall vortex flow direction, which promotes the high-velocity coolant near the target wall developing downstream. Therefore, the Coriolis force will provide a more intense of heat transfer of the *IVC* in SS-side-in than that in PS-side-in, and this effect will be more intensify under higher rotating speed.

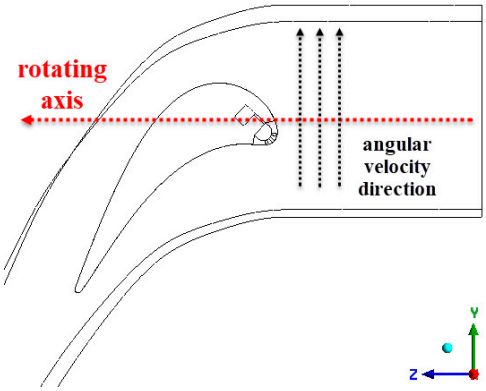

(a) Sketch of the rotating axis and angular velocity direction.

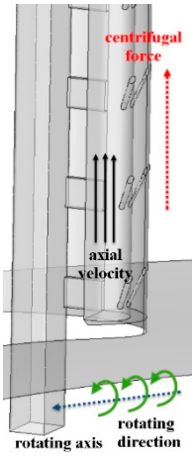

(b) Sketch of the axial velocity and centrifugal force direction.

Preprints (www.preprints.org) | NOT PEER-REVIEWED | Posted: 28 July 2023 doi:10.20944/preprints202307.1983.v1

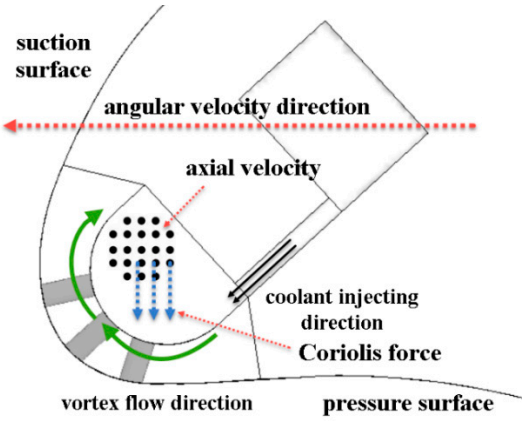

(c) Sketch of the Coriolis force effect on the vortex flow in the case of PS-side-in.

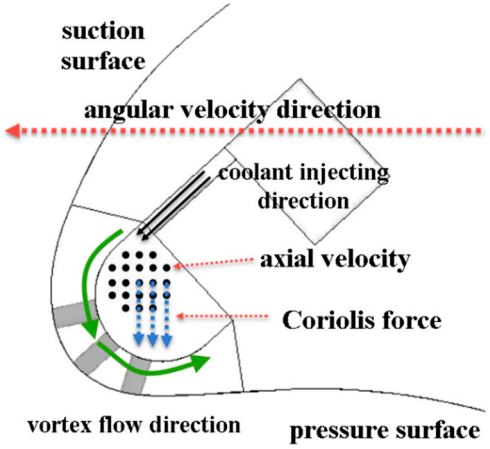

(d) Sketch of the Coriolis force effect on the vortex flow in the case of SS-side-in.

Figure 16. Sketch of the Coriolis force effect on the *IVC* flow.

Figure 17 exhibits the Nusselt contour on the target surface in the PS-side-in and SS-side-in. It can be noticed that the high-*Nu* region originating from the nozzle develops downstream and covers a relatively larger area in the SS-side-in compared to that in the PS-side-in region at 1500-3000rpm. In addition, the angular velocity ω and the axial velocity $\boldsymbol{V}_r$ close to the shroud region are higher than the other regions in the vortex chamber. Thus, the Coriolis force effect on the vortex flow will be more intense close to the shroud region, resulting in higher *Nu* around the shroud region in the SS-side-in as compared to PS-side-in. Given the coolant flow is unable to flow axially out of the vortex chamber through the shroud wall, there will be flow blockage near the shroud region. Together with the effect of the high-pressure *MF* outer flow, the intensity of the vortex flow heat transfer close to the shroud region in PS-side-in will be weakened. This explained the phenomenon shown in Figure 12 that large-area of high temperature regions appear near the shroud region in PS-side-in rather than that in SS-side-in. Another noteworthy observation is the high-*Nu* region close to the film holes. This heat transfer enhancement phenomenon is brought about by the "suction effect" as discussed before.

Preprints (www.preprints.org) | NOT PEER-REVIEWED | Posted: 28 July 2023 doi:10.20944/preprints202307.1983.v1

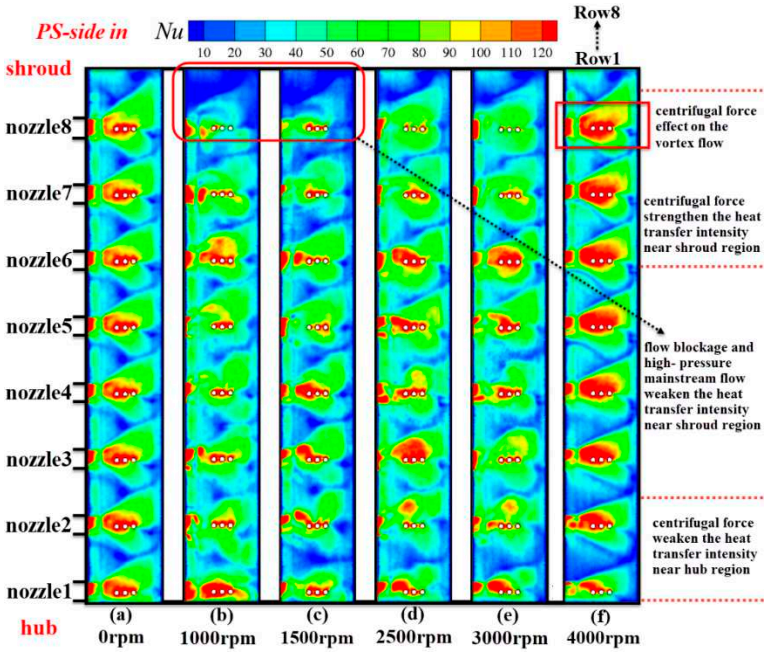

(1) PS-side in

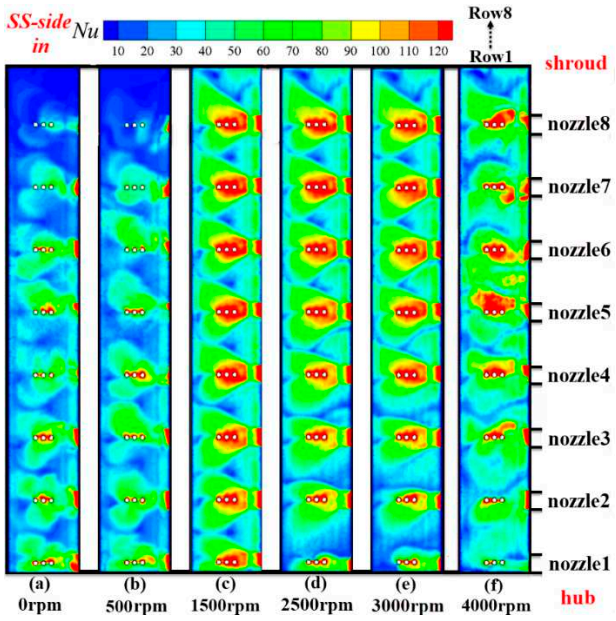

(2) SS-side in

Figure 17. *Nu* contour on the target wall in the case of SS-side-in .vs. PS-side-in.

To sum up, the arrangement of the coolant injecting nozzles makes a difference in the interaction between the Coriolis force and the internal vortex flow. The nozzle position will significantly impact the intensity of the internal heat transfer, and change the overall VFCC performance. The nozzles arranged near the pressure surface side is recommended to the turbines running under relatively low rotating speed range. And the nozzles arranged near the suction surface side is recommend for the relatively high rotating speed conditions. Such conclusion cannot be drawn in the IVC research under the symmetrical MF as in the past work or neglecting the MF effects.

Previous studies, including Li et al. [21] and Wang et al. [16], have evaluated the performance of VFCC in BLE by separately analyzing the effectiveness θ of the EFC as well as the heat transfer intensity (Nu) of the IVC. However, these studies were carried out under the adiabatic conditions, so a higher value for both θ and Nu was considered indicative of superior performance of a specified

Preprints (www.preprints.org) | NOT PEER-REVIEWED | Posted: 28 July 2023 doi:10.20944/preprints202307.1983.v1

VFCC. In the present research, we found that the BLE surface temperature is affected by the heat conduction between IVC flow and the external film coolant coverage within conjugate approach. The higher intensity of the internal heat transfer results in the lower actual temperature on the BLE surface. However, a lower intensity of the internal heat transfer does not necessarily mean a higher actual temperature on the BLE surface. This is because better coolant film coverage on the BLE surface and lower internal heat transfer intensity can also lead to relatively better cooling performance. Therefore, when heat conduction brought about by the blade material is taken into consideration, the temperature on the BLE surface will be the more reasonable criterion for evaluation as compared to Nu.

To properly evaluate the cooling concept performance, it's important to consider the flow loss and heat transfer situation simultaneously. Shevchuk et al. [22] have proposed an aerodynamic parameter that takes into account both the heat transfer situation and pressure loss. The defination of this aerodynamic parameter is defined as:

$$\Phi = (Nu_a/Nu_0) / ((f / f_0)^{(1/3)}) \quad (4)$$

Nu_a represents the area-averaged Nusselt number on the target wall of the vortex chamber.

$Nu_0 = 0.023Re_D^{0.8}Pr^{0.4}$ stands for the Dittus-Boelter correlation of the smooth channel axial flow, in Nu_0:

- $Re_D = \rho UD_c/\mu$ (U stands for the average axial velocity of the vortex flow)
- Pr stands for the Prandtl Number

$f_0 = 0.184Re_D^{-0.2}$ means the Blasius friction

$f = 2\ (P_{in}-P_{out})\ D_c/(\rho V_j^2 L)$ stands for the loss of pressure, in f:

- P_{out} stands for the mean pressure of the film hole channel internal side
- P_{in} stands for the mean pressure of the coolant flow at internal inlet
- V_j stands for the velocity of the coolant flow at internal inlet
- D_c means the cross-section hydraulic diameter of the vortex chamber
- T_w represents the target wall temperature
- ρ represents the fluid density
- L represents the vortex chamber axial length

The aim of incorporating cooling structures in turbine blades is to lower temperature of the blade and prevent thermal damage while minimizing coolant usage. Thus, in equation (4), we can replace Nusselt number Nu with the delta on the BLE surface. Similarly, friction factor f can be substituted with the mass flow of the coolant at the internal inlet M_c. This approach yields a more appropriate criterion φ for assessing the impact of rotation on the performance of VFCC in engineering application scenarios:

$$\varphi = (\theta_a / \theta_0) / ((M_c / M_{c0})^{(1/n)}) \quad (5)$$

where:

- θ_a means *delta* on the *BLE* surface (area-averaged value)
- θ_0 means *delta* on the *BLE* surface (area-averaged value) at stationary case (0 rpm)
- M_c means the mass flow of the coolant flow at the internal inlet
- M_{c0} means the mass flow of the coolant flow at the internal inlet at stationary case (0 rpm)
- n is the alterable weighting index whose meaning is provided in the following text

A higher delta on the blade surface (namely a lower blade surface temperature) together with a lower consumption of the coolant air means a higher value of VFCC performance parameter φ. By adjusting the value of n, engineers can modify this criteria used to evaluate cooling performance. When n is relatively higher, the temperature of the blade surface becomes the more important criterion, while when n is relatively lower, the coolant consumption takes on greater significance. Tables 3 and 4 show the value of φ for n = 3 in the case of PS-side-in and SS-side-in, respectively.

Preprints (www.preprints.org) | NOT PEER-REVIEWED | Posted: 28 July 2023 doi:10.20944/preprints202307.1983.v1

Table 3. Aerodynamic parameters of PS-side-in.

ω/rpm	0	500	1000	1500	2000	2500	3000	3500	4000
θ_a	0.3831	0.3895	0.3901	0.4101	0.3960	0.3802	0.4038	0.3960	0.3938
M_c/M_{c0}	1.000	1.001	1.394	0.592	0.396	1.620	1.833	2.813	3.010
φ	1.00	1.02	0.91	1.27	1.41	0.84	0.86	0.73	0.71

Table 4. Aerodynamic parameters of SS-side-in.

ω/rpm	0	500	1000	1500	2000	2500	3000	3500	4000
θ_a	0.2791	0.2883	0.3746	0.4082	0.4025	0.3946	0.4066	0.4269	0.4047
M_c/M_{c0}	1.289	1.988	1.673	1.023	1.024	1.023	1.125	1.954	0.735
φ	0.67	0.60	0.82	1.06	1.04	1.02	1.02	0.89	1.17

It's evident that coolant consumption rises steeply with the growing rotating speed. When the SL is positioned near RowP, coolant consumption is considerably lower at 1500rpm and 3000rpm. The SS-side-in shows superior cooling performance to the PS-side-in under the relatively high rotating speed. These findings hold true for the cooling structure examined in this study.

Our goal is to examine how rotational effects impact the characteristics of the composite conjugate cooling. Given that various sorts of gas turbines have their own designated rotating speeds, it's important to conduct more thorough simulations within specific ranges of rotating speeds while designing the BLE cooling conceptions such as the VFCC structures for various gas turbine applications (air, sea, land).

4. Conclusion

In this study, the impacts of rotation and the coolant injecting nozzle position on the characteristics of the vortex and film composite conjugate cooling are explored under the *MF* within practical cases. The governing equations solved in the numerical simulations are the three-dimensional steady RANS coupled with SST~γ-θ. Additionally, incorporating blade material solid region into the internal cooling structure brings about the fluid-thermal coupling. By comparing coolant injecting nozzles placed near the pressure surface side (PS-side-in) versus the suction surface side (SS-side-in), we can analyze how *EFC* flow interacts with *IVC* flow, and how rotation affects *IVC* flow. We also define the dimensionless temperature θ for analysis, which varies inversely with temperature.

In terms of the *MF*, the position of the *SL* is the main factor brought about by the rotation. When the position of the *SL* aligns with the film holes, coolant jet that flows from film holes is suppressed effectively onto the blade surface, providing extensive coverage and resulting in a lower temperature distribution on the blade surface. On the other hand, when the *SL* remains in other positions, the coolant film lifts off from the blade surface, leading to a higher blade surface temperature. However, the impact of nozzle position on coolant film attachment is not easily discernible.

For the *IVC* the centrifugal force as a result of the rotation makes the coolant move axially. The axial velocity and the angular velocity bring about the Coriolis force. The direction of the Coriolis force is opposite and similar to the near-wall vortex flow direction in the PS-side-in and SS-side-in, respectively. This makes the internal heat transfer intensity in SS-side-in case higher than that in PS-side-in under high rotating speed, leading to a lower temperature of the blade surface in SS-side-in with the heat conduction brought about by the blade material.

Given the comparison of the aerodynamic parameter involving both the *BLE* surface temperature and the coolant consumption, the nozzles arranged near the pressure surface side is recommended to the turbines running under relatively low rotating speed range. And the nozzles arranged near the suction surface side is suggested to the relatively high rotating speed conditions.

Preprints (www.preprints.org) | NOT PEER-REVIEWED | Posted: 28 July 2023 doi:10.20944/preprints202307.1983.v1

Author Contributions: Jiefeng Wang: Conceived and designed the analysis, Collected the data, Performed the analysis, Wrote the paper; Eddie Yin Kwee NG: Conceived and designed the analysis, Revised the paper; Jianwu Li: Collected the data; Yanhao Cao: Collected the data; Yanan Huang: Collected the data; Liang Li: Conceived and designed the analysis, Revised the paper.

Funding: This work was supported by the [National Science and Technology Major Project] under Grant [2017-I-0009-0010].

Conflicts of Interest: The authors declare no conflict of interest.

References

1. HAN J-C, DUTTA S, EKKAD S. Gas Turbine Heat Transfer and Cooling Technology [M]. Taylor & Francis, Boca Raton, FL 33487-2742, 2012.
2. KREITH F, SONJU O. The Decay of a Turbulent Swirl in a Pipe [J]. Journal of Fluid Mechanics, 1965, 22(02): 257-271.
3. LING J P, IRELAND P T, HARVEY N W. Measurement of heat transfer coefficient distributions and flow field in a model of a turbine blade cooling passage with tangential injection; proceedings of the ASME Turbo Expo 2006: Power for Land, Sea, and Air, Barcelona, Spain, F, 2006 [C]. American Society of Mechanical Engineers.
4. DU C, LI L, WU X, *et al*. Effect of jet nozzle geometry on flow and heat transfer performance of vortex cooling for gas turbine blade leading edge [J]. Applied Thermal Engineering, 2015, 93: 1020-1032.
5. DU C, LI L, CHEN X X, *et al*. *Nu*merical Study on Effects of Jet Nozzle Angle and *Nu*mber on Vortex Cooling Behavior for Gas Turbine Blade Leading Edge; proceedings of the ASME Turbo Expo 2016: Turbomachinery Technical Conference and Exposition, Seoul, South Korea, F, 2016 [C].
6. FAN X, LI L, ZOU J, *et al*. Local heat transfer of vortex cooling with multiple tangential nozzles in a gas turbine blade leading edge cooling passage [J]. International Journal of Heat and Mass Transfer, 2018, 126: 377-389.
7. WANG J, DU C, WU F, *et al*. Investigation of the vortex cooling flow and heat transfer behavior in variable cross-section vortex chambers for gas turbine blade leading edge [J]. International Communications in Heat and Mass Transfer, 2019, 108: 104301.
8. ZHAO H-J, JIANG Y-T, ZHENG Q, *et al*. Particle Deposition Characteristics of U-Shaped Rib Channel of Marine Gas Turbine [J]. Tuijin Jishu/Journal of Propulsion Technology, 2021, 42(8): 1906-1914.
9. ZHU X-D, ZHANG J-Z, TAN X-M. *Nu*merical assessment of round-to-slot film cooling performances on a turbine blade under engine representative conditions [J]. International Communications in Heat and Mass Transfer, 2019, 100: 98-110.
10. YE L, LIU C, DU K, *et al*. Influences of groove configuration and density ratio on grooved leading-edge showerhead film cooling using the pressure sensitive paint measurement technique [J]. Int J Heat Mass Tran, 2022, 190: 122641.
11. YE L, LIU C, LI B, *et al*. Detailed showerhead cooling effectiveness measurements on the notched leading-edge surface: Effect of freestream turbulence and density ratio [J]. International Communications in Heat and Mass Transfer, 2022, 135: 106142.
12. FAN X, DU C, LI L, *et al*. *Nu*merical simulation on effects of film hole geometry and mass flow on vortex cooling behavior for gas turbine blade leading edge [J]. Applied Thermal Engineering, 2016, 112: 472-483.
13. DU C, LI L, FAN X, *et al*. Rotational influences on aerodynamic and heat transfer behavior of gas turbine blade vortex cooling with bleed holes [J]. Applied Thermal Engineering, 2017, 121: 302-313.
14. LI L, DU C H, CHEN X X, *et al*. *Nu*merical study on flow and heat transfer behavior of vortex and film composite cooling [J]. Journal of Mechanical Science and Technology, 2018, 32(6): 2905-2917.

Preprints (www.preprints.org) | NOT PEER-REVIEWED | Posted: 28 July 2023 doi:10.20944/preprints202307.1983.v1

15. ZHANG M, WANG N, HAN J-C. Internal heat transfer of film-cooled leading edge model with normal and tangential impinging jets [J]. Int J Heat Mass Tran, 2019, 139: 193-204.
16. WANG J, LI L, LI J, *et al*. *Nu*merical investigation on flow and heat transfer characteristics of vortex cooling in an actual film-cooled leading edge [J]. Applied Thermal Engineering, 2021, 185: 115942.
17. TIMKO L. Energy efficient engine high pressure turbine component test performance report [R], 1984. NASA-CR-168289, https://ntrs.nasa.gov/citations/19900019237
18. CELIK I B, GHIA U, ROACHE P J, *et al*. Procedure for estimation and reporting of uncertainty due to discretization in CFD applications [J]. Journal of fluids Engineering-Transactions of the ASME, 2008, 130(7): 078001.
19. KOHLI A, BOGARD D. Adiabatic effectiveness, thermal fields, and velocity fields for film cooling with large angle injection [J]. 1997, 119(2): 352-358.
20. SAFI A, HAMDAN M O, ELNAJJAR E. *Nu*merical investigation on the effect of rotation on impingement cooling of the gas turbine leading edge [J]. Alexandria Engineering Journal, 2020, 59(5): 3781-3797.
21. LI L, DU C, CHEN X, *et al*. *Nu*merical study on flow and heat transfer behavior of vortex and film composite cooling [J]. Journal of Mechanical Science and Technology, 2018, 32(6): 2905-2917.
22. SHEVCHUK I V, JENKINS S C, WEIGAND B, *et al*. Validation and analysis of *Nu*merical results for a varying aspect ratio two-pass internal cooling channel [J]. Journal of heat transfer, 2011, 133(5): 1085-1094.

Disclaimer/Publisher's Note: The statements, opinions and data contained in all publications are solely those of the individual author(s) and contributor(s) and not of MDPI and/or the editor(s). MDPI and/or the editor(s) disclaim responsibility for any injury to people or property resulting from any ideas, methods, instructions or products referred to in the content.